




Essay

Surrogate-Model-Based Interval Analysis of Spherical Conformal Array Antenna with Power Pattern Tolerance

Guangda Ding ¹, Peng Li ^{1,*}, Paolo Rocca ^{1,2}, Jiantao Chang ^{1,*} and Wanye Xu ¹

¹ The Key Laboratory of Electronic Equipment Structure Design, Ministry of Education, Xidian University, Xi'an 710071, China

² The ELEDIA Research Center, ELEDIA@UniTN—University of Trento, Via Sommarive 9, 38123 Trento, Italy

* Correspondence: yinhong0523@163.com (P.L.); taocj@xidian.edu.cn (J.C.)

Abstract: A method based on an interval arithmetic is proposed to analyze uncertain factors such as the curvature radii, excitation amplitude, and excitation phase of a spherical conformal array antenna. An interval description of element factors under different curvature radii of spherical substrates is established using the surrogate model based on the data obtained through a full-wave analysis method. The interval formula of the spherical curvature radius and array element position error is derived and the effects of the spherical radius tolerance, excitation amplitude tolerance, and excitation phase tolerance on the antenna power pattern are studied. To evaluate the effectiveness and reliability of the proposed method, a set of representative numerical results are reported and discussed and a comparison with the Monte Carlo methods and full-wave simulation is described. This method can be widely used during the antenna design and before the antenna prototyping/manufacturing to predict the effects, on the radiation performance, of possible errors/tolerances in the antenna structure to guarantee the antenna working ‘in operation’.

Keywords: interval arithmetic; surrogate model; spherical conformal array antenna; tolerance analysis



Citation: Ding, G.; Li, P.; Rocca, P.; Chang, J.; Xu, W.

Surrogate-Model-Based Interval Analysis of Spherical Conformal Array Antenna with Power Pattern Tolerance. *Sensors* **2022**, *22*, 9828. <https://doi.org/10.3390/s22249828>

Academic Editor: Vittorio Rampa

Received: 14 November 2022

Accepted: 12 December 2022

Published: 14 December 2022

Publisher's Note: MDPI stays neutral with regard to jurisdictional claims in published maps and institutional affiliations.



Copyright: © 2022 by the authors. Licensee MDPI, Basel, Switzerland. This article is an open access article distributed under the terms and conditions of the Creative Commons Attribution (CC BY) license (<https://creativecommons.org/licenses/by/4.0/>).

1. Introduction

Conformal array antennas (CAAs) refer to an array antenna attached to and fitted to a carrier surface, i.e., a non-planar conformal antenna array that needs to be conformally installed on a fixed-shape surface [1]. The patch array antenna is widely used in aerospace [2,3] and military [4] communication equipment owing to its high gain characteristics, flexible shape, controllable beam shape, and ease in conforming to the surfaces of dielectric substrate.

To meet the aerodynamic requirements of aircraft, CAAs usually have a special shape that incorporates the shape of an airborne radome [5]. Compared with array antennas, whose traditional plane configurations severely limit their application in aircraft with curved shapes, CAAs have the feasibility of a joint other physical geometry, space saving, increased array aperture, and reduced aerodynamic drag, greatly improving the space utilization and stealth performance of a carrier [6–8]. Therefore, the realization of conformal array antennas has significant potential in future applications, which has attracted the attention of scholars [9]. Ma et al. designed and manufactured a curved dielectric plate antenna that can provide a wider bandwidth and a higher gain [10]. Ramadan et al. also studied a wearable conical antenna and controlled its RF performance while maintaining the flexibility of the antenna [11]. With the wide application of conformal antennas, 3D printing technology provides a channel for the processing of antenna models. As a disadvantage, the accuracy is slightly inferior to that of the traditional chemical etching method [12]. Therefore, it is necessary to explore the influence of uncertain factors of the antenna structure on its power pattern.

Uncertain factors of array antennas, mainly structural and system factors, affect the actual performance of the antenna. Therefore, an interval analysis of the electrical performance can be carried out according to uncertain factors of the antenna. There are two main methods of interval analysis: probability- and improbability-based research methods [13,14]. Based on the research method of probability, Ruze was the first to study the influence of aperture tolerance on antenna radiation patterns, taking the uncertainty variable as a Gaussian distribution for research by analyzing a large number of statistical data [15,16]. Gilbert studied the influence of random geometric errors on antenna pattern gain [17]. Elliott analyzed the influence of random errors in the structure and excitation on the sidelobe level; this method can only analyze the influence of random errors on a certain electrical performance [18]. Samii proposes a research based on Ruze that considers non-uniform root mean square surface error and non-uniform illumination function at the same time to determine the influence of different random errors and illumination taper on parameters such as gain loss and sidelobe level [19,20]. Hsiao used statistical methods to study the relationship between random error and maximum sidelobe level, which is of great significance in radar systems [21,22]. Ling studied the probability distribution of reflector antenna sidelobe levels affected by some random surface errors [20]. With the development of the antenna model toward a higher precision, this method requires a lot of time and numerous resources. Therefore, more researchers now choose such methods based on probability.

Research methods based on improbability mainly consider interval arithmetic (IA) and have been well developed in recent years [23–26]. In general, the upper and lower bounds of the variables are easily obtained through a small number of experiments and, thus, the interval arithmetic treats the uncertain factors as interval variables. Rocca et al. exploited an interval analysis method to explore the influence of the uncertainties of array factors on the power pattern of an array antenna, including the excitation amplitude tolerance [27–29] and the excitation phase tolerance [30,31]; when the excitation distribution is known, the variation range of the radiation pattern is deduced by the interval expression. Later, Anselmi et al. studied the influence of the excitation amplitude and phase errors on the radiation pattern of the array antenna based on the interval center and radius [28,30], which laid a foundation for a subsequent interval analysis. Li et al. used interval analysis arithmetic to study the influence of radome uncertainties on the far-field pattern, including the radome thickness [32] and permittivity of the materials [33]. Wang et al. studied the tolerance of a 3D-printed patch antenna and proved that the influence of the element and array factors on the power pattern cannot be ignored [34].

To the best of the authors' knowledge, (1) considering only the tolerance analysis of planar array antennas in the existing works, this study focuses on the effects of the structural and excitation tolerance on the power pattern of spherical CAAs; (2) considering only the tolerance of the array factor, the tolerances in both element factor and array factor could be researched by this study. Based on the IA method, according to the geometric characteristics of the sphere, the formula of the element position, excitation amplitude, phase, and pattern of the CAAs are derived. The interval of the element factors under different radii of a spherical substrate is established using a surrogate model to describe the data obtained by the full-wave analysis method. Finally, the influence of the uncertain factors of the CAAs on the antenna power pattern is studied based on the element and array factors.

The remainder of this paper is organized as follows. The theoretical formula for a spherical CAA is derived in Section 2. Some numerical examples are used to verify the validity and accuracy of the proposed method in Section 3. Section 4 describes the analyses and studies the uncertain factors of the CAA. Finally, some conclusions are drawn in Section 5.

2. Materials Formula

For linear array and planar array, the beam direction of each directional element is the same if the same element is used. According to the pattern product theorem [35], the array pattern can be expressed in the form of the product of element factors fa and array factors fe , as shown in (1).

$$F(\theta, \varphi) = fa(\theta, \varphi) \cdot fe(\theta, \varphi) \quad (1)$$

Since the elements of conformal array are distributed on the surface of the carrier and the direction of the pattern of each directional element is different, the multiplication principle similar to the linear array cannot be simply used to solve the pattern. The pattern of conformal array antenna will be analyzed below.

As shown in Figure 1a, for N-element arbitrary antenna array in space, let the position of the n th array element at r_n in the array be (x_n, y_n, z_n) and the excitation of the array element be $w_n = A_n e^{jB_n}$. A_n is the excitation amplitude and B_n is the excitation phase. For observation point P in the far field (θ, φ) , the direction vector is

$$\alpha = (\cos \phi \sin \theta, \sin \phi \cos \theta, \cos \theta) \quad (2)$$

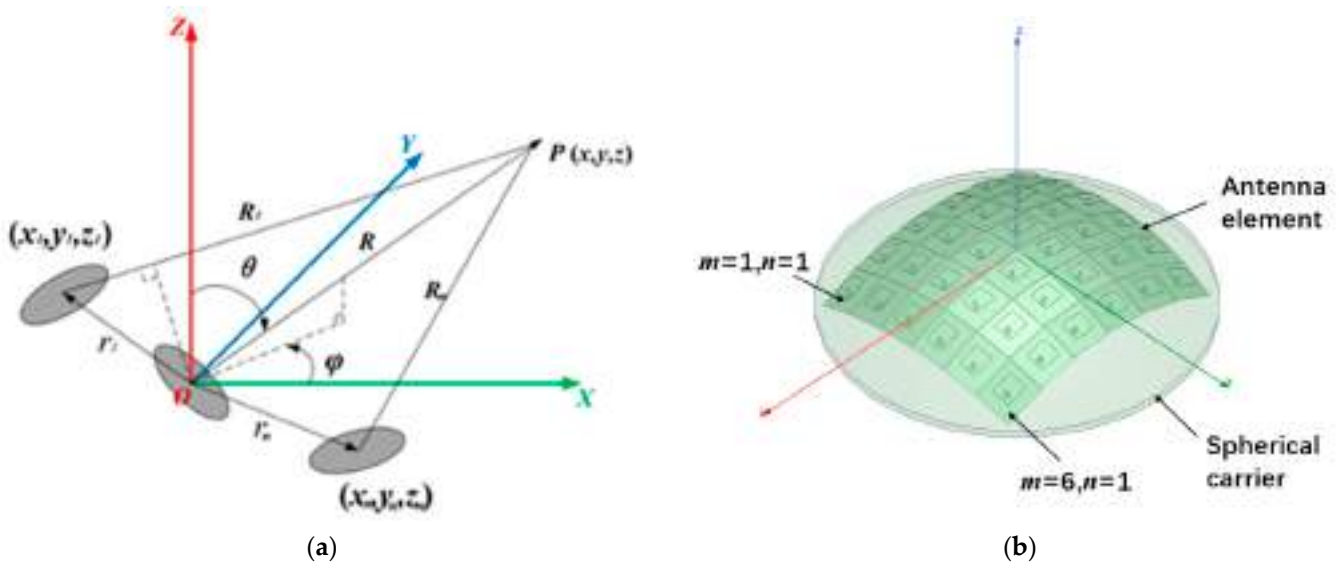


Figure 1. Simple model and spatial placement model of 3D conformal array antenna ((a) diagram of space conformal array antenna, (b) model diagram established by HFSS).

With the coordinate origin O as the phase reference point, the path difference between the element arriving at far-field point P and the reference point arriving at point P is

$$d_n = r_n \cdot \alpha = x_n \cos \phi \sin \theta + y_n \sin \phi \cos \theta + z_n \cos \theta \quad (3)$$

The radiation pattern of the n th antenna array element at point P can be expressed as

$$F_n(\theta, \varphi) = f_n(\theta, \varphi) \cdot w_n \cdot e^{jk d_n} \quad (4)$$

where $f_n(\theta, \varphi)$ is the element pattern of the n th array element. According to the superposition principle of electromagnetic field, the far-field radiation pattern of this N-element array is

$$\begin{aligned} F(\theta, \varphi) &= \sum_{n=1}^N F_n(\theta, \varphi) = \sum_{n=1}^N f_n(\theta, \varphi) \cdot w_n \cdot e^{jk d_n} \\ &= \sum_{n=1}^N f_n(\theta, \varphi) \cdot A_n \cdot e^{j(B_n + k(x_n \cos \phi \sin \theta + y_n \sin \phi \cos \theta + z_n \cos \theta))} \end{aligned} \quad (5)$$

2.1. Array Factors of Spherical CAAs

The derivation of the array factor needs to start from the calculation of the coordinates of the central point of each element. Because of the perfect spatial symmetry of the spherical array structure, it can be regarded as consisting of several ring arrays, and the radius of each ring is determined by its position distribution on the sphere. Taking the $m \times n$ CAA in Figure 2 as an example (the radius of the sphere is R_s), where α is the angle between the two antenna elements relative to the origin of the coordinate and it is related to the length and width of the element patch antenna. α_m represents the angle between the m th row antenna and the x -axis on the plane and α_n represents the angle between the n th column antenna element and the y -axis on the yoz plane. α_m and α_n are angles calculated based on the number of elements and the spherical radius $\alpha_m = 1/2(\pi - (m - 1)\alpha)$ and $\alpha_n = 1/2(\pi - (n - 1)\alpha)$. Therefore, the position of the center point of the antenna element in the m th row and n th column can be calculated based on the geometric relationship of the sphere.

$$\begin{aligned} R_m &= R_s \times \cos(\pi/2 - \alpha_m) \\ x_{mn} &= R_s \times \sin(\pi/2 - \alpha_m) \\ y_{mn} &= R_m \times \cos \alpha_n \\ z_{mn} &= R_m \times \sin \alpha_n \end{aligned} \quad (6)$$

where R_m represents the radius on the xoz plane of the antenna in the m th row.

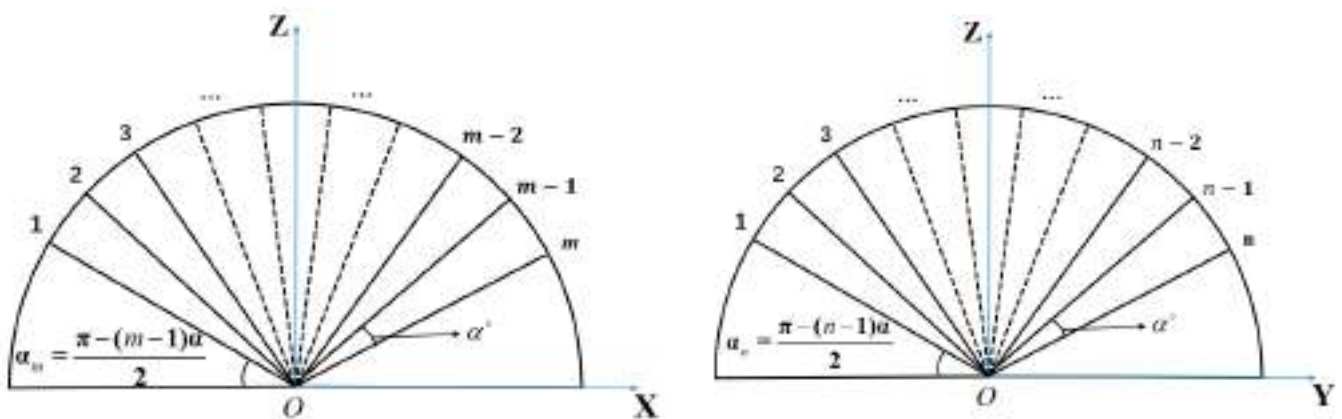


Figure 2. $m \times n$ spherical CAA angle calculation model.

For spherical CAAs, all antenna elements were distributed in a three-dimensional (3D) space, as shown in Figure 1. The position of each antenna element is different in the 3D cartesian coordinate system. The far radiation field of the antenna element is the product of the vector pattern of the antenna element and the spherical wave $e^{-jk_0 R_{mn}} / R_{mn}$. The radiation far field of the antenna element after approximate processing can be expressed as follows in spherical coordinate system [36]:

$$\begin{aligned} E_{mn}(\theta, \varphi, r) &= A \cdot f e_{mn}(\theta, \varphi) \frac{e^{-jk_0 R_{mn}}}{R_{mn}} \\ &= \frac{e^{-jkR}}{R} f e_{mn}(\theta, \varphi) e^{jkr_{mn} \cdot \hat{r}} \end{aligned} \quad (7)$$

where r_{mn} is the position vector of the element antennas in the m th row and n th column relative to the origin O of the 3D cartesian coordinate system, \hat{r} is the unit vector in the $P(x, y, z)$ direction at some point in the far field. Here, is the coordinate transformation between the two coordinate systems, $r_{mn} = x_{mn}\hat{x} + y_{mn}\hat{y} + z_{mn}\hat{z}$, $\hat{r} = u\hat{x} + v\hat{y} + \cos\theta\hat{z}$, where $u = \cos\varphi \sin\theta$ and $v = \sin\varphi \sin\theta$. A is a constant, which is usually omitted in the analysis of array antennas. Therefore, the array factor of the CAAs obtained from the

superposition theorem is as follows. It is the closed-form equation of array factor fa and spherical radius r .

$$fa(\theta, \varphi) = \sum_{m=1}^M \sum_{n=1}^N w_{mn} e^{jk_0(ux_{mn} + vy_{mn} + \cos\theta z_{mn})} \quad (8)$$

2.2. Establishment of Element Factor Interval Surrogate Model Based on Machine Learning

The patch antenna is widely used as the element in array antenna. The pattern (element factor) formula of traditional planar patch antenna can be found in much of the literature [12,34]. The tolerance analysis of structure factor such as dimensions and materials based on IA has also been conducted in [34], however it cannot be used for the spherical patch antenna of CAAs due to the limitations of the theoretical formula. Therefore, this section uses the surrogate model obtained by the method of artificial intelligence to overcome the theoretical derivation of a closed-form formula for the spherical patch antenna pattern, just as the Taylor series has been used as the surrogate model to replace the rigorous theoretical deduction and reduce the overestimate of IA in [34,37,38].

The process of obtaining the surrogate model is shown in Figure 3. Firstly, the full wave analysis method (HFSS) was used to establish the element model of conformal patch antenna. Then, the interval of the spherical patch antenna pattern with a structure tolerance interval was obtained by the Monte Carlo (MC) method and the data were calculated via HFSS used for training and validation and new data predictions using a backpropagation (BP) neural network. Finally, the data were sorted and normalized and the upper and lower boundary formulas of element factors were fitted in MATLAB. Here, R_s represents the radius of the spherical substrate, the subscript *inf* in $R_s \in [R_{s_{inf}}, R_{s_{sup}}]$ represents the lower boundary, and *sup* represents the upper boundary.

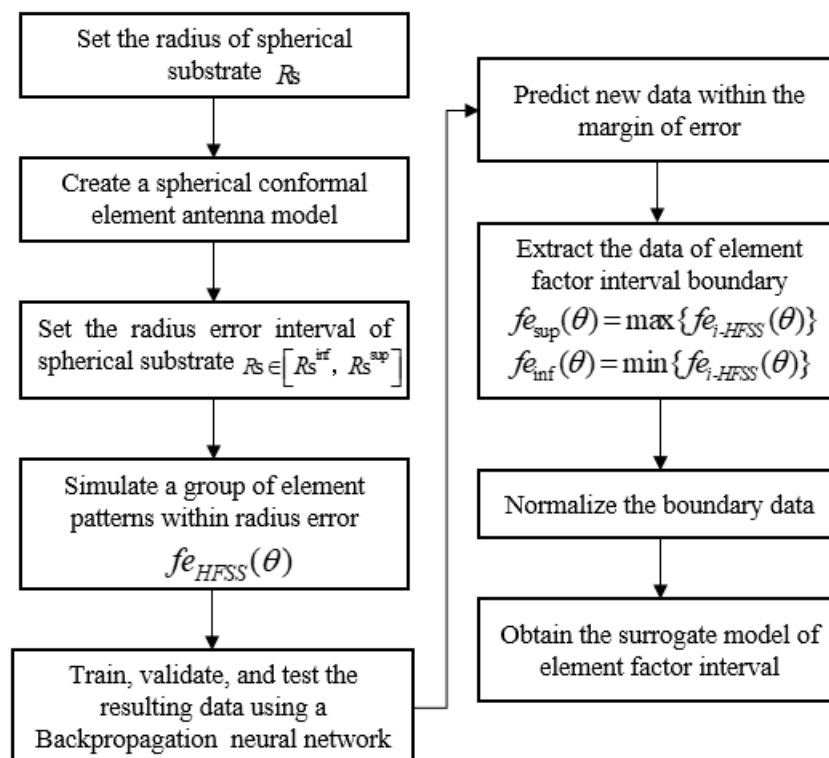


Figure 3. The flow chart of the surrogate model.

The BP neural network is a multi-layer feedforward network trained according to the error backpropagation algorithm and it is also one of the most widely used neural network models. The basic structure of a neuron is shown in Figure 4, which consists of an input layer, a hidden layer, and an output layer. Nodes (neurons) relate to some specified

weights. Using the BP trained network to predict new data can not only obtain accurate data but can also save a lot of time in HFSS simulation. As shown in Figure 5, the green line represents the E-plane/H-plane pattern under different radii within a group of radius errors simulated using the BP neural network; the maximum $f_{e-HFSS}(\theta)$ and minimum $f_{e-HFSS}(\theta)$ values of the corresponding angle points in this group of data are proposed as the upper boundary $f_{e_{sup}}(\theta)$ (red line) and lower boundary $f_{e_{inf}}(\theta)$ (blue line) of the element factor interval. Finally, the upper and lower boundaries were fitted using MATLAB to obtain the approximate function about θ as the surrogate model of the element factor. The midpoint and radius were used to represent the element factor interval as follows [28].

$$\begin{aligned} f_{e_{sup}}(\theta) &= \max\{f_{e-HFSS}(\theta)\} \\ f_{e_{inf}}(\theta) &= \min\{f_{e-HFSS}(\theta)\} \quad i = 1, 2, \dots, n \end{aligned} \tag{9}$$

where i represents the number of simulations in HFSS, $\theta \in (-90^\circ, 90^\circ)$ and then $f_{e_{mid}} = 1/2 \times (f_{e_{inf}} + f_{e_{sup}})$ and $f_{e_{rad}} = 1/2 \times (f_{e_{sup}} - f_{e_{inf}})$; here the subscripts *mid* and *rad* (the same below) represent the midpoint and radius of the interval, respectively.

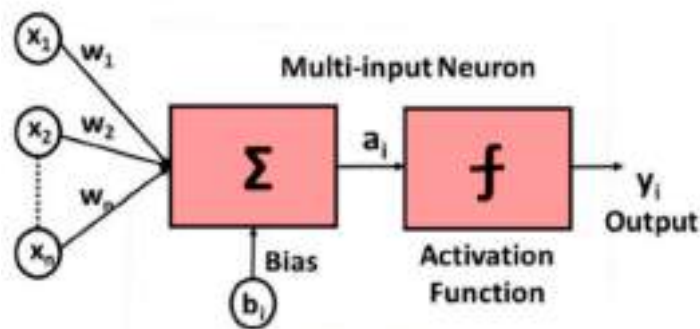


Figure 4. Basic structure of a neuron.

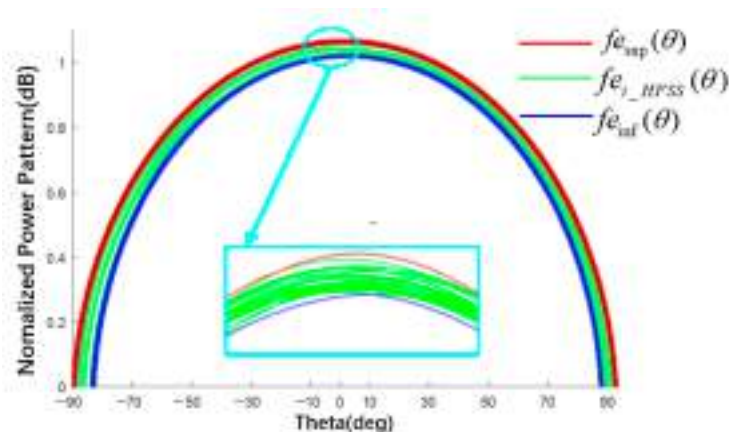


Figure 5. Element pattern (schematic of surrogate model for obtaining the element factor interval).

2.3. Internal Power Pattern of Spherical CAAs

After the formula of the element factor $f_e(\theta, \varphi)$ and array factor $f_a(\theta, \varphi)$ of CAAs is obtained, the far-field pattern of the CAAs can be expressed as (5) and substituted into $P(\theta, \varphi) = |F(\theta, \varphi)|^2$ to calculate the power pattern.

$$F(\theta, \varphi) = \sum_{m=1}^N \sum_{n=1}^N w_{mn} f_{e_{mn}}(\theta, \varphi) \times \sin(a_n) e^{jk_0(ux_{mn} + vy_{mn} + \cos\theta z_{mn})} \tag{10}$$

The requested steps to obtain the bounds of power pattern from the radius error intervals are shown in Figure 6. After determining the tolerance range of the radius of the

spherical substrate, we can obtain the boundary of the coordinate of the center point of the antenna element according to the geometric relationship between the center point of the antenna element and the spherical radius in the cartesian coordinate system and we can substitute it and the element factor surrogate model into (5) to obtain the boundary of the far-field pattern. Then, it can be expanded into real part and imaginary part and divided into many cases to solve the boundary of power pattern.

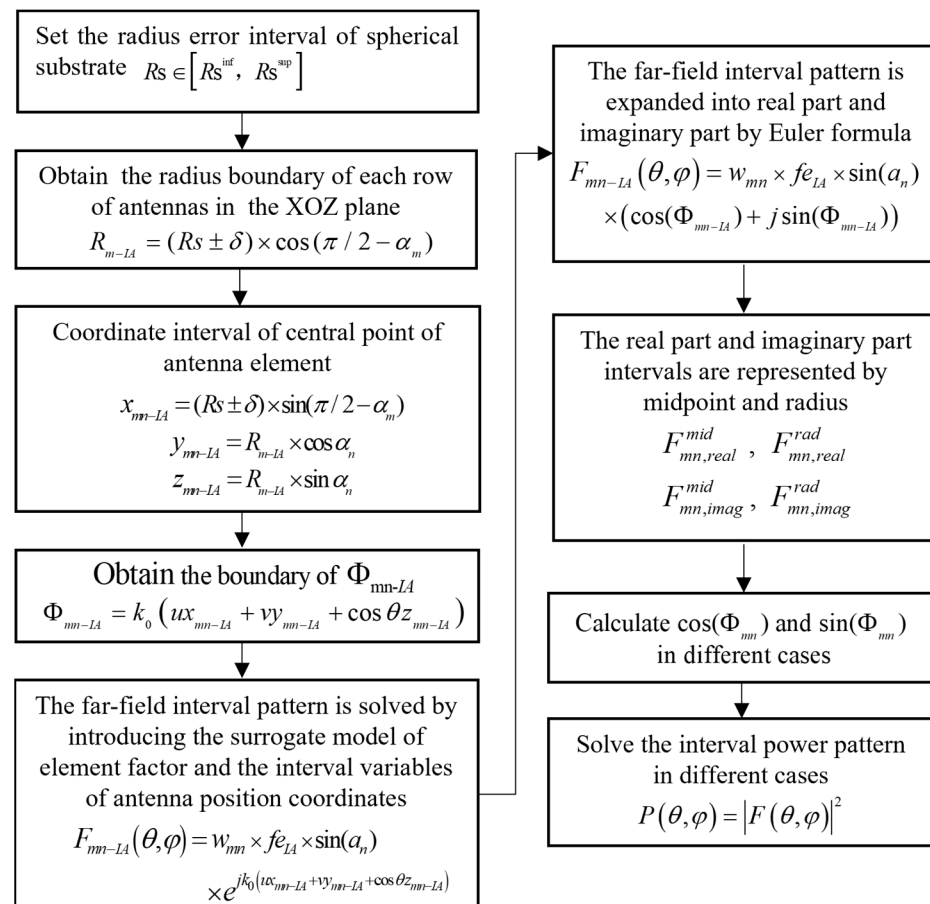


Figure 6. The flow chart for solving the interval power pattern.

When there is a tolerance, it is assumed that the element factor of each element antenna in the array antenna has the same upper and lower boundaries; then the interval formula for the m th row and n th column element pattern is shown in (11), where the subscript IA represents the interval value (the same as below) and $fe_{IA}(\theta, \varphi) \times \sin(a_n)$ indicates that the element factor interval takes the component on the z -axis.

$$F_{m-IA}(\theta, \varphi) = w_{mn} fe_{IA}(\theta, \varphi) \times \sin(a_n) \times e^{jk_0(ux_{m-IA} + vy_{m-IA} + \cos \theta z_{m-IA})} \quad (11)$$

The radius of curvature of the m th antenna on the xoz plane is expressed as follows:

$$R_{m-IA} = (R_s \pm \delta) \times \cos(\pi/2 - \alpha_m) \quad (12)$$

The x -, y -, and z -axis coordinates of the center point of the patch antenna element in the m th are expressed as:

$$\begin{aligned} x_{m-IA} &= (R_s \pm \delta) \times \sin(\pi/2 - \alpha_m) = x_{mn-mid} \pm x_{mn-rad} \\ y_{m-IA} &= R_{m-IA} \times \cos \alpha_n = y_{mn-mid} \pm y_{mn-rad} \\ z_{m-IA} &= R_{m-IA} \times \sin \alpha_n = z_{mn-mid} \pm z_{mn-rad} \end{aligned} \quad (13)$$

The central coordinate position of the element is located in the exponent part in (11) and can be replaced by Φ_{mn} :

$$\begin{aligned}
 \Phi_{mn-inf} &= k_0(ux_{mn-inf} + vy_{mn-inf} + \cos \theta z_{mn-inf}) \\
 \Phi_{mn-sup} &= k_0(ux_{mn-sup} + vy_{mn-sup} + \cos \theta z_{mn-sup}) \\
 \Phi_{mn-mid} &= k_0(ux_{mn-mid} + vy_{mn-mid} + \cos \theta z_{mn-mid}) \\
 \Phi_{mn-rad} &= 1/2 \times (\Phi_{mn-sup} - \Phi_{mn-inf})
 \end{aligned}
 \tag{14}$$

The array pattern is the sum of all element patterns, as shown in (15):

$$F_{IA}(\theta, \varphi) = \sum_{m=1}^N \sum_{n=1}^N F_{mn-IA}(\theta, \varphi)
 \tag{15}$$

The interval formulas of (15) is obtained as follows via the midpoint and radius notation in interval theory [39].

$$\begin{aligned}
 F_{mn,real}^{mid} &= A_{mn} \sin(a_n) \times \mu\{fe_{-IA}\} \times \mu\{\cos(\Phi_{mn})\} \\
 F_{mn,real}^{rad} &= A_{mn} \sin(a_n) \times \left(\begin{aligned} &|\mu\{fe_{-IA}\}| \times \frac{1}{2}\omega\{\cos(\Phi_{mn})\} + |\mu\{\cos(\Phi_{mn})\}| \\ &\times \frac{1}{2}\omega\{fe_{-IA}\} + \frac{1}{2}\omega\{fe_{-IA}\} \times \frac{1}{2}\omega\{\cos(\Phi_{mn})\} \end{aligned} \right)
 \end{aligned}
 \tag{16}$$

$$\begin{aligned}
 F_{mn,imag}^{mid} &= A_{mn} \sin(a_n) \times \mu\{fe_{-IA}\} \times \mu\{\sin(\Phi_{mn})\} \\
 F_{mn,imag}^{rad} &= A_{mn} \sin(a_n) \times \left(\begin{aligned} &|\mu\{fe_{-IA}\}| \times \frac{1}{2}\omega\{\sin(\Phi_{mn})\} + |\mu\{\sin(\Phi_{mn})\}| \\ &\times \frac{1}{2}\omega\{fe_{-IA}\} + \frac{1}{2}\omega\{fe_{-IA}\} \times \frac{1}{2}\omega\{\sin(\Phi_{mn})\} \end{aligned} \right)
 \end{aligned}
 \tag{17}$$

where μ represents the midpoint, ω represents the interval width, and the subscripts *real* and *imag* represent the real and imaginary parts of the complex item, respectively. The interval calculation of $\cos(\Phi_{mn})$ and $\sin(\Phi_{mn})$ are used in the method in [32]; then the upper and lower boundaries of the power pattern interval of CAAs are as indicated in (18) and (19), respectively.

$$P_{Rs}^{inf} = \begin{cases} \min \left((F_{real}^{inf})^2, (F_{real}^{sup})^2 \right) + \min \left((F_{imag}^{inf})^2, (F_{imag}^{sup})^2 \right); \\ \quad (F_{real}^{inf} > 0 || F_{real}^{sup} < 0) \&\& (F_{imag}^{inf} > 0 || (F_{imag}^{sup}) < 0) \\ \min \left((F_{real}^{inf})^2, (F_{real}^{sup})^2 \right); \\ \quad (F_{real}^{inf} > 0 || F_{real}^{sup} < 0) \&\& (F_{imag}^{inf} \le 0 || (F_{imag}^{sup}) \ge 0) \\ \min \left((F_{imag}^{inf})^2, (F_{imag}^{sup})^2 \right); \\ \quad (F_{real}^{inf} \le 0 || F_{real}^{sup} \ge 0) \&\& (F_{imag}^{inf} > 0 || (F_{imag}^{sup}) < 0) \\ 0; \textit{Otherwise} \end{cases}
 \tag{18}$$

$$P_{Rs}^{sup} = \max \left((F_{real}^{inf})^2, (F_{real}^{sup})^2 \right) + \max \left((F_{imag}^{inf})^2, (F_{imag}^{sup})^2 \right)
 \tag{19}$$

In addition to the structural uncertainty analysis of the element factors in the CAAs, the interval analysis of the excitation error on the electrical performance can also be discussed via the proposed method. Based on (10), the excitation amplitude is taken as the interval variable, as shown in (20). The influence of the tolerance of the excitation amplitude on the electrical performance of the antenna can be further studied.

$$\begin{aligned}
 F(\theta, \varphi) &= \sum_{m=1}^N \sum_{n=1}^N A_{mn-IA} \times fe_{mn}(\theta, \varphi) \times \sin(a_n) e^{jk_0(ux_{mn} + vy_{mn} + \cos \theta z_{mn})} \\
 A_{mn-IA} &= [A_{mn} - \delta \times A_{mn}, A_{mn} + \delta \times A_{mn}]
 \end{aligned}
 \tag{20}$$

Based on (5), the excitation phase is taken as the interval variable, as shown in (21), where $B_{mn} = [B_{mn}^{\text{inf}}; B_{mn}^{\text{sup}}]$ is the phase error of the CAAs, with the upper and low boundaries $B_{mn}^{\text{inf}} = b_{mn} - \beta$ and $B_{mn}^{\text{sup}} = b_{mn} + \beta$, respectively, and β is the phase error (unit = degree). Similarly, the interval analysis method RIA in [13] substitutes (21) into the interval formula of the power pattern to obtain the upper and lower boundaries.

$$F(\theta, \varphi) = \sum_{m=1}^N \sum_{n=1}^N A_{mn} f_{e_{mn}}(\theta, \varphi) \times \sin(a_n) e^{j[k_0(ux_{mn} + vy_{mn} + \cos \theta z_{mn}) + B_{mn}]} \quad (21)$$

Because the phase and radii errors are located in the exponent part, they can also be expressed by Φ_{mn} , as shown in (22).

$$\Phi_{mn} = k_0(ux_{mn} + vy_{mn} + \cos \theta z_{mn}) + B_{mn} \quad (22)$$

3. Numerical Examples of Verification

3.1. Verification of Spherical Element Factors

This section tries to verify the surrogate model of the spherical element factor (spherical patch antenna pattern). The patch antenna (as element) is designed and simulated by full-wave method (HFSS) as shown in Figure 7. The radius of the spherical substrate is an interval variable; it is 500 mm with an error of 1.5 mm, the length of the patch is $L = 41$ mm, the width is $W = 41$ mm, the distance from the bottom feed to the center is 6.5 mm, the permittivity is 2.2, and the thickness of the substrate is 2 mm. It is assumed that the radius of curvature at any point of the antenna element is the same, there is no radius distribution in the patch, and the radius of the different element antennas can be different. When there is an error in the radius of the spherical substrate, the corresponding element factor is affected but the upper and lower boundaries of all antenna element patterns are consistent.

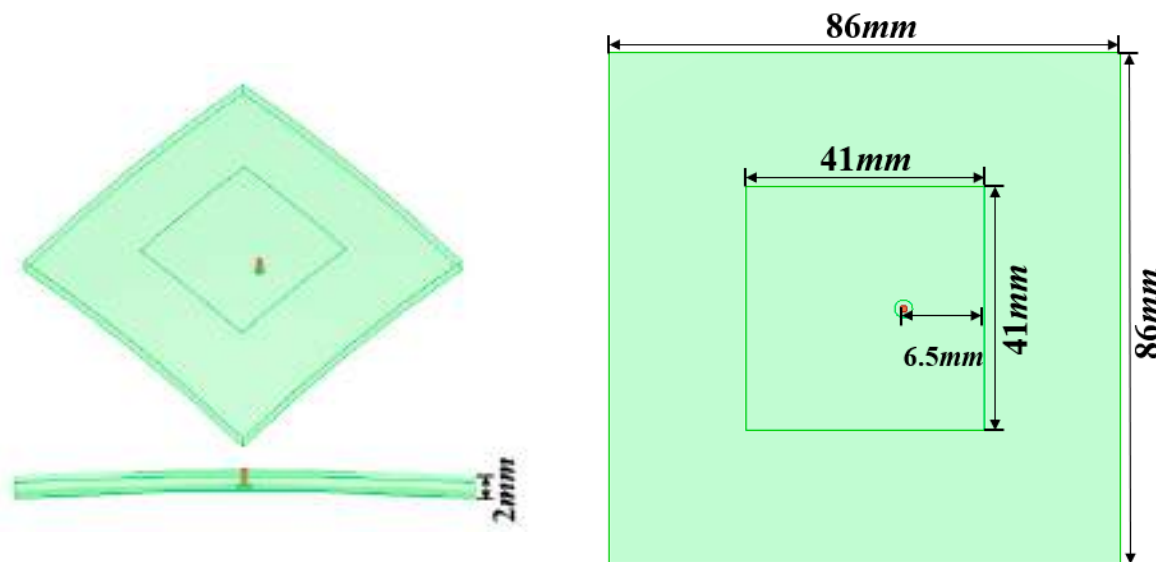


Figure 7. Model of conformal patch antenna.

There are two parameters used for BP neural network training in this research: spherical substrate radius and radiation angle. The spherical substrate radius error samples simulated in HFSS are 31 (498.5 mm–501.5 mm, with an interval of 0.1 mm) and 1801 radiation angle samples (-90° – 90° , with an interval of 0.1°). These two samples are combined and 55,831 databases were generated. The database is randomly forked and the ratios of 80%, 10%, and 10% are used for training, validation, and testing, respectively. The comparison between the actual value and the predicted value is shown in Figure 8. When the number of nodes in the middle-hidden layer is 10, the mean square error at this time is

0.0276. Therefore, the prediction of new data within the error range can be made using the trained network.

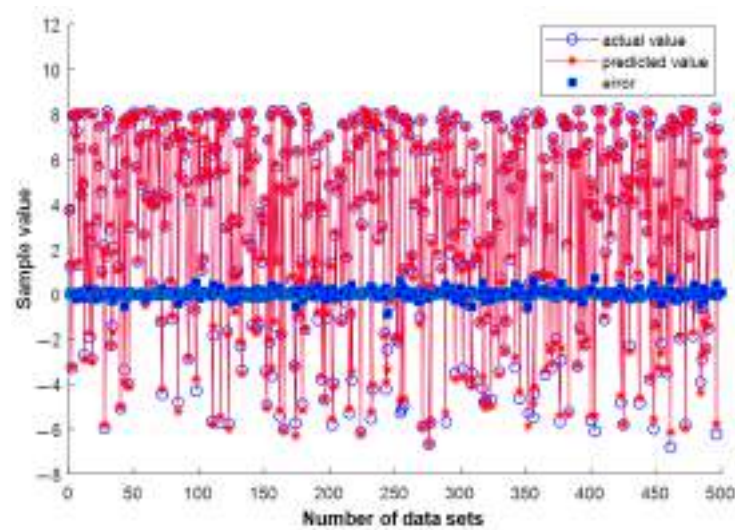


Figure 8. Comparison of predicted value and actual value of BP neural network test set.

Taking the E-plane element pattern as an example, the element factor pattern interval obtained by the surrogate model is shown in Figure 9. The green line is the MC simulation result of the trained BP neural network (200 times in total) with radius varies in interval [498.5, 501.5] mm randomly, and the red and blue lines are the upper and lower boundaries fitted by MATLAB. The fitting accuracy of MATLAB was 10^{-25} . The normalized element factor interval is listed in Table 1, where Δ represents the interval width. The interval obtained by MATLAB completely envelops all simulation results of the BP.

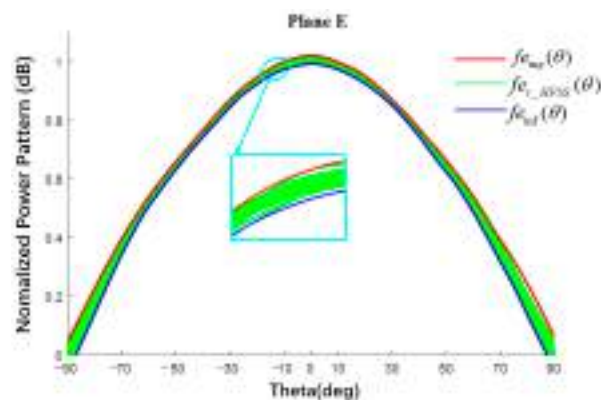


Figure 9. Interval pattern of E-plane element factor.

Table 1. Interval value of element factor of plane E in Figure 9.

Theta (Deg)	BP Results	Δ	This Work	Δ
−60	[0.507; 0.540]	0.033	[0.507; 0.541]	0.034
−30	[0.847; 0.868]	0.021	[0.843; 0.870]	0.027
0	[0.993; 1.015]	0.022	[0.991; 1.020]	0.029
30	[0.850; 0.869]	0.019	[0.850; 0.870]	0.020
60	[0.489; 0.536]	0.047	[0.487; 0.541]	0.054

3.2. Verification of Planar Arrays

The power pattern of a planar array obtained by the proposed method was compared with the results of a full-wave method (HFSS). A 10×10 array antenna was taken as

an example and the radius of the spherical substrate was set to infinity. The calculation results were compared with the array antenna simulated using HFSS software, as shown in Figures 10 and 11.

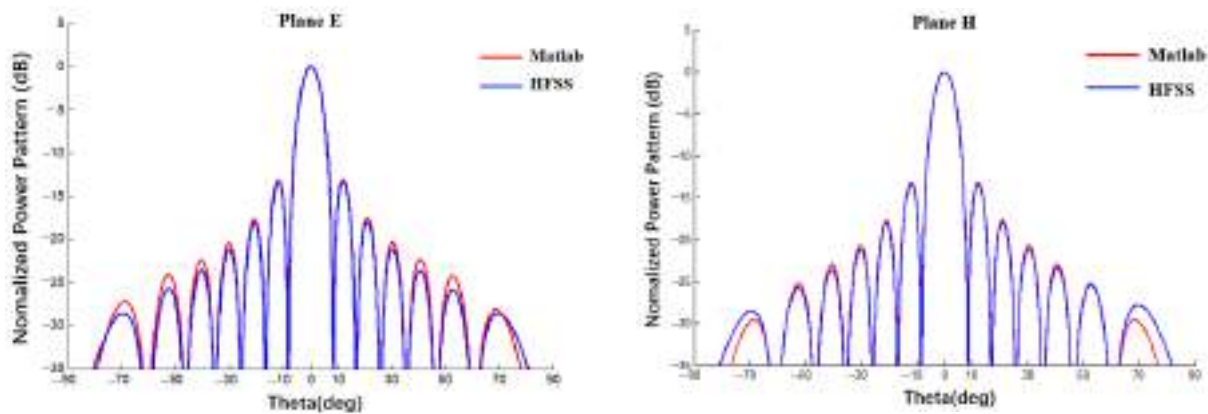


Figure 10. Simulation of 10×10 array antenna contrast pattern using MATLAB and HFSS (uniform excitation).

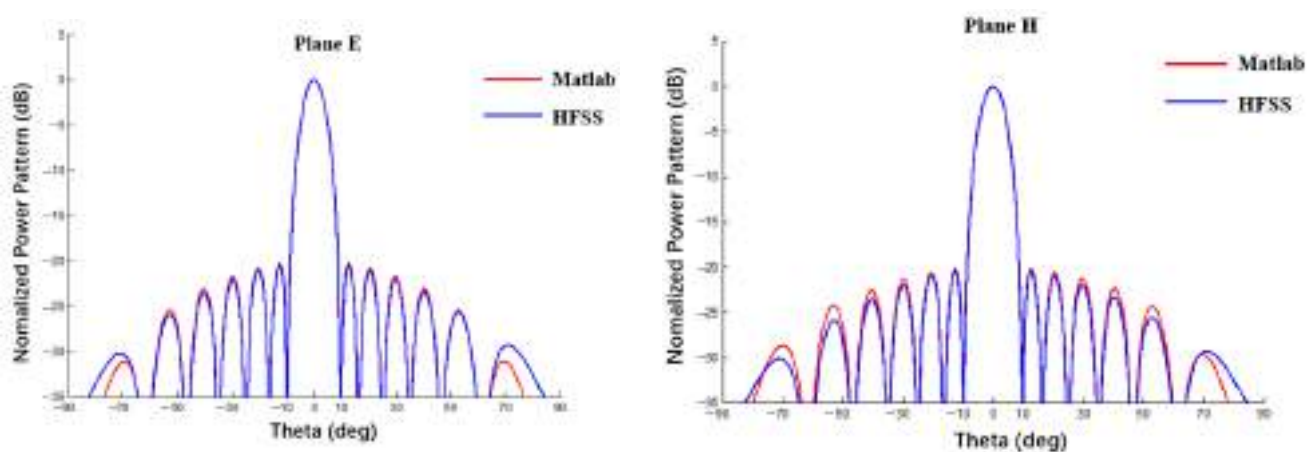


Figure 11. Simulation of 10×10 array antenna contrast pattern using MATLAB and HFSS (Dolph-Chebyshev excitation).

It can be seen from Figures 10 and 11 that, when the radius of the spherical substrate is sufficiently large, the two power patterns are almost the same and, the closer they are to the main lobe, the closer they are numerically. At a distance from the main lobe, the two patterns are slightly different. It is undeniable that the surrogate model of the element factor obtained by fitting will also incur an error. In addition, the pattern obtained through the proposed method is asymmetrical in the far-side lobes, mainly because the pattern of the element factor obtained by BP neural network is not completely symmetrical, as shown in Figure 9. Then, the examples in Section A and B can prove that the surrogate model can obtain satisfactory calculation accuracy and can be used for the tolerance analysis with high efficiency rather than a full-wave method such as HFSS.

3.3. Verification of Spherical Array

This section verifies the proposed method in a spherical conformal array antenna. A 6×6 spherical CAA as shown in Figure 1 was designed and simulated by the full-wave method (HFSS). The radius of the spherical substrate was 1000 mm and three cases were compared with the power pattern calculated by HFSS, as shown in Figure 12. Case 1 (blue line): with reference to the method in [28], the element factor was not included and only the array factor was taken into account. Case 2 (red line): with reference to the method in [34],

the element and array factors were considered simultaneously and the element factor used the theoretical formula of a planar patch antenna. Case 3 (black line): using the method proposed in this work, the element and array factors were considered simultaneously and the surrogate model of the element factor was obtained using the HFSS data.

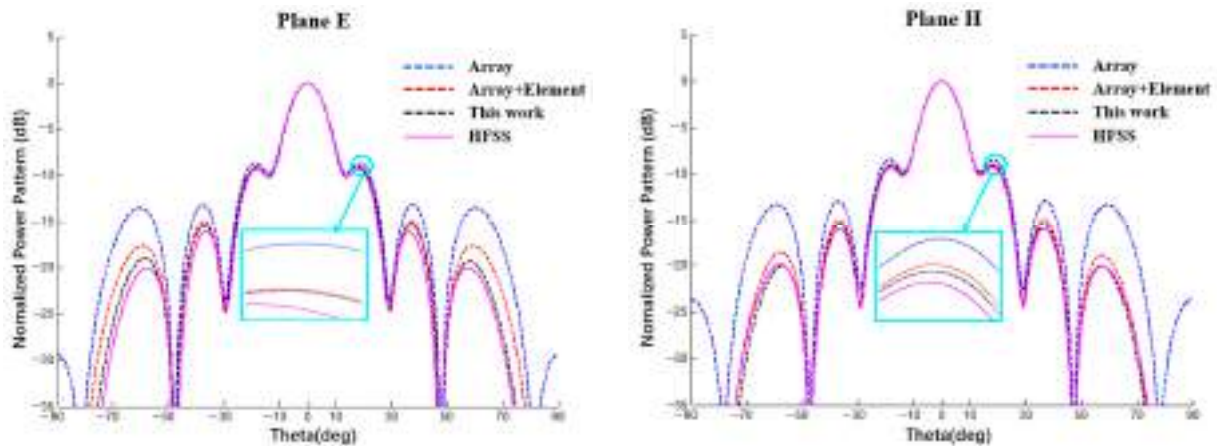


Figure 12. Comparison of simulation results between HFSS and MATLAB (Plane E, uniform excitation).

In Figure 12, the pink line represents the results obtained through the full-wave method (HFSS), it can be seen that the power pattern trends of the HFSS results are completely consistent, among which the difference between the simulation results of the HFSS with only an array factor is the largest, particularly in the far lobe region. The element factor has a significant effect on the power pattern. The difference between the results of the proposed method and the HFSS results is minimal, which demonstrates the reliability and effectiveness of the proposed method.

3.4. Verification of Linear/Planar Arrays Interval Analysis

When the spherical radius is sufficiently large, the curved surface tends toward the plane. When the element number m or n is set to 1, this method is also applicable to linear arrays. To verify the proposed interval analysis method of CAAs, a comparison between a spherical substrate with a sufficiently large radius and the planar/linear array antenna is also one of the verification examples. The tolerance analysis of a linear array was implemented in this section and results obtained by this method are compared with data in [28,30]. The results in the presence of the excitation amplitude and phase tolerance are shown in Figures 13 and 14. A data comparison with the literature [28,30] is shown in Tables 2 and 3.

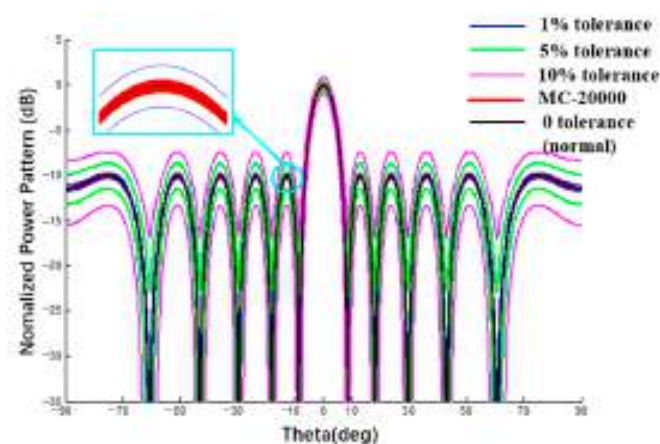


Figure 13. Linear array antenna pattern with excitation amplitude tolerance (Plane E, Dolph-Chebyshev excitation, the tolerance of MC method is 1%).

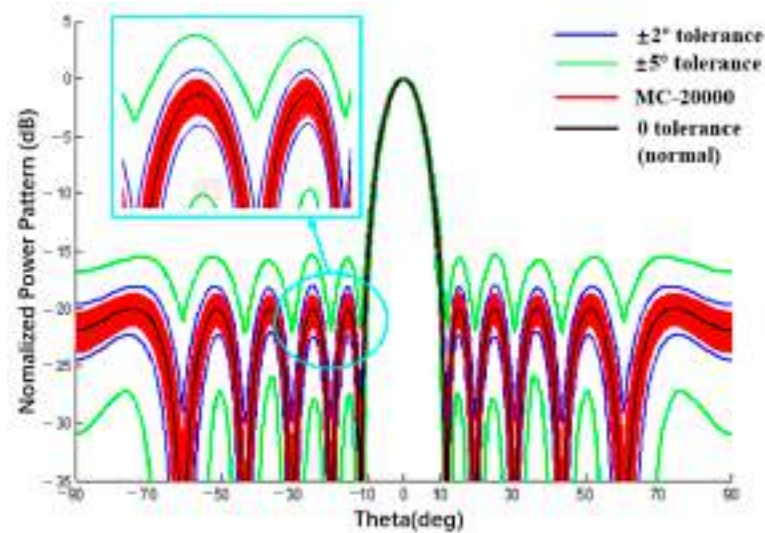


Figure 14. Linear array antenna pattern with excitation phase tolerance (Plane E, Dolph–Chebyshev excitation, the tolerance of MC method is $\pm 2^\circ$).

Table 2. Numerical results of power pattern in Figures 13 and 15.

SLL(dB)	Amplitude Error	Line Array (Figure 13)	ΔL	Curvilinear Array (Figure 15)	ΔC	[28]	Δ
−10	1%	[−10.28; −9.64]	0.64	[−3.08; −2.58]	0.50	[−10.29; −9.68]	0.61
	5%	[−11.51; −8.42]	3.09	[−4.15; −1.62]	2.53	[−11.49; −8.43]	3.06
	10%	[−13.11; −6.89]	6.22	[−5.56; −0.53]	5.03	[−13.10; −6.96]	6.14

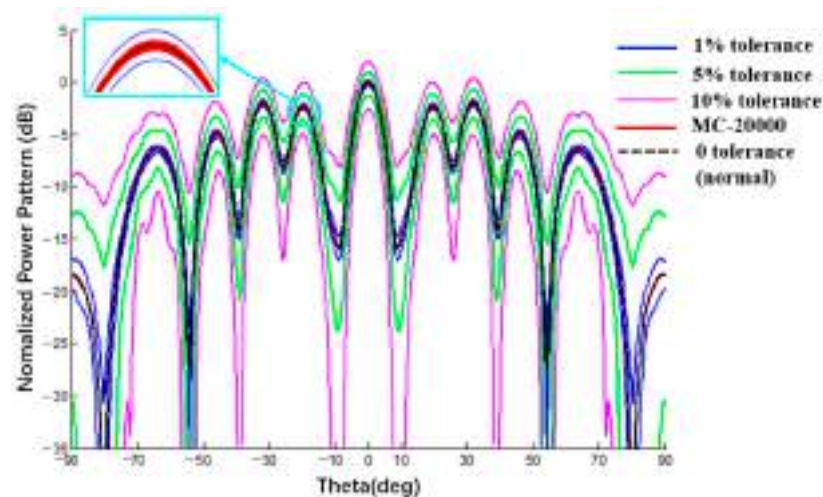


Figure 15. Power pattern under different excitation amplitude tolerances (Plane E, Dolph–Chebyshev excitation, the tolerance of MC method is 1%).

Table 3. Numerical results of power pattern in Figures 14 and 16.

SLL (dB)	Phase Error	Line Array (Figure 14)	ΔL	Curvilinear Array (Figure 16)	ΔC	[30]	Δ
−20	2°	[−21.06; −18.92]	2.14	[−3.30; −1.91]	1.39	[−20.58; −18.42]	2.16
	5°	[−26.30; −15.97]	10.33	[−4.50; −0.99]	3.51	[−25.45; −14.81]	10.64

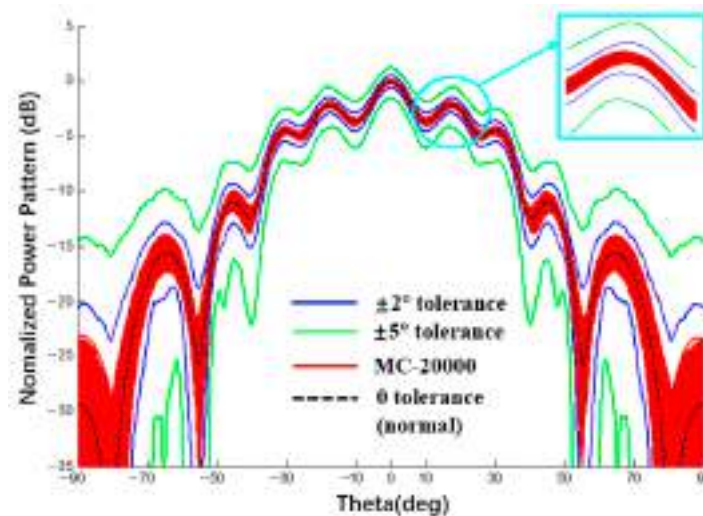


Figure 16. Power pattern under different excitation phase tolerances (Plane E, Dolph–Chebyshev excitation, the tolerance of MC method is $\pm 2^\circ$).

In the first example, the Dolph–Chebyshev excitation is adopted and the error of excitation amplitude is 1%, 5%, and 10%, respectively. Comparing the interval width of the proposed method and RIA [29], the two values are very close, which can prove that the tolerance analysis results of the amplitude error interval by the proposed method are reasonable.

In the second example, the sidelobe level (SLL) is -20 dB, the excitation mode is the same as the example in [30], and the phase error is 2 and 5 deg. Comparing the interval width of the proposed method and RIA [30], the two values are almost the same, which proves that the tolerance analysis results of the phase error interval by the proposed method are also reasonable.

3.5. Verification of Conformal Arrays Interval Analysis

Because there is no comparable interval analysis example for a spherical CAA, the interval results of the linear array on the spherical surface were compared with the results of the plane linear array and the MC method. The radius of the spherical substrate is 500 mm and its ideal power pattern and the pattern with excitation amplitude and phase error are shown in Figures 15 and 16. Table 2 was compared with the example with the amplitude error interval in [28]. The comparison conditions in the two works are the same, i.e., SLL = -10 dB, Dolph–Chebyshev excitation is applied, and the amplitude error ratios are 1%, 5%, and 10%, respectively. A spherical CAA significantly increased the sidelobe. Comparing the interval width of this method and RIA [28], the two results are of the same order of magnitude, which proves that the data calculated by the proposed method are reasonable.

Table 3 was compared with the example with the phase error interval in [30]. The comparison conditions in the two works are the same, i.e., SLL = -20 dB, Dolph–Chebyshev excitation is applied, and the phase error is 2 deg and 5 deg. The interval width between the method in this study and RIA [31] was compared. Although the interval width obtained by the proposed method is less than that of the RIA [31], it is still of the same order of magnitude. Therefore, it can be proved that the phase error data calculated by the proposed method are reasonable.

4. Tolerance Analysis of Spherical CAAs with Error Interval

In this section, a tolerance analysis carried out for the spherical CAAs with radius, excitation amplitude, and phase error intervals is described.

4.1. Tolerance Analysis of Spherical CAA with Radius Error Interval

The 6×6 array antenna in Figure 1 was also taken as an example. Under uniform excitation, the spherical substrate radius is 500 mm and the error of the radius error is $\{\pm 0.5, \pm 1.0, \pm 1.5\}$ mm. The selected 6×6 array is completely symmetrical and the patterns of the E- and H-planes are roughly the same. Therefore, the analysis results of the E-plane power pattern are shown in Figures 17 and 18 and compared with the results of 20,000 Monte Carlo simulations. The results are listed in Table 4. In addition, we also used the Ruze formula ($G = G_0 e^{-(4\pi\delta_{rms}/\lambda)^2}$) to calculate the gain deviation under different error conditions for comparison with the interval gain pattern calculated by this study method [16]. When the errors are 0.5 mm, 1 mm, and 1.5 mm, the gain deviations calculated by the Ruze formula are -0.042 dB, -0.168 dB, and -0.379 dB, respectively, while the deviation intervals obtained in this study are $[-0.66; 0.66]$ dB, $[-1.05; 1.02]$ dB, and $[-1.52; 1.37]$ dB. The peak deviation estimated by the Ruze formula are all within the interval obtained by this study method.

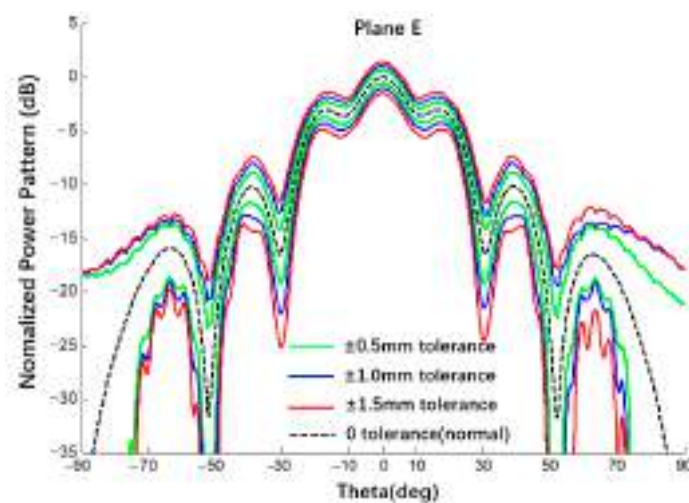


Figure 17. Interval power pattern of radius error of spherical CAAs (Plane E, uniform excitation).

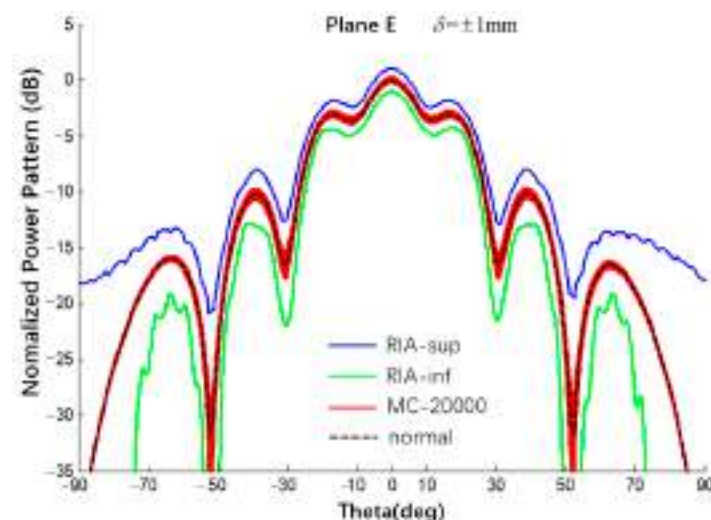


Figure 18. Interval power pattern of radius error of spherical CAAs (Plane E, uniform excitation, the tolerance of MC method is ± 1 mm).

Table 4. Numerical results of SLL of power pattern in Figures 17 and 18.

Radius Error		± 0.5 mm	$\Delta 0.5$	± 1.0 mm	$\Delta 1.0$	± 1.5 mm	$\Delta 1.5$
Main 0 dB	This Work	[−0.66; 0.66]	1.32	[−1.05; 1.02]	2.07	[−1.52; 1.37]	2.89
	MC	[−0.13; 0.14]	0.27	[−0.23; 0.28]	0.51	[−0.38; 0.42]	0.80
1st −3.09 dB	This Work	[−3.80; −2.35]	1.45	[−4.34; −1.87]	2.47	[−4.90; −1.42]	3.48
	MC	[−3.26; −2.92]	0.34	[−3.40; −2.74]	0.66	[−3.57; −2.60]	0.97

4.2. Tolerance Analysis of Spherical CAA with Excitation Amplitude Error Interval

Using the same spherical CAAs with a uniform excitation and an amplitude error of $\delta = \{1\%, 3\%, 5\%\}$ and comparing via Monte Carlo results (20,000 times), the interval results of the E-plane power pattern of the spherical CAA were obtained, as shown in Figures 19 and 20 and listed in Table 5.

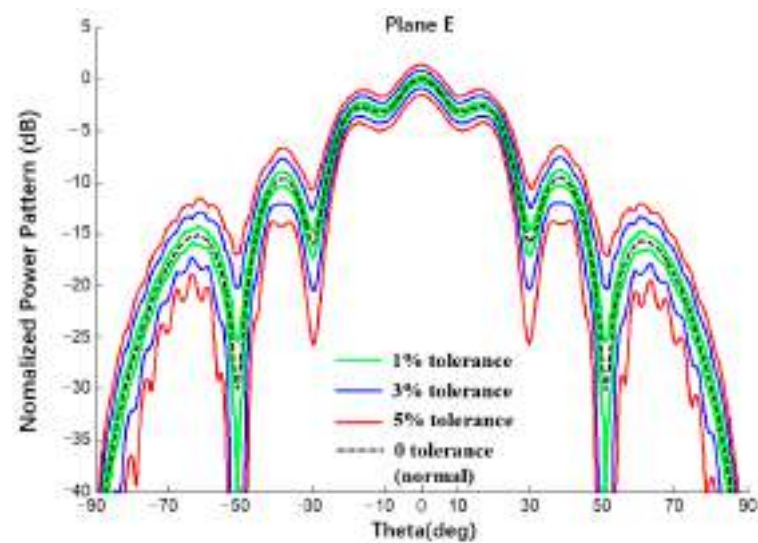


Figure 19. Interval power pattern of excitation amplitude error of spherical CAAs (Plane E, uniform excitation).

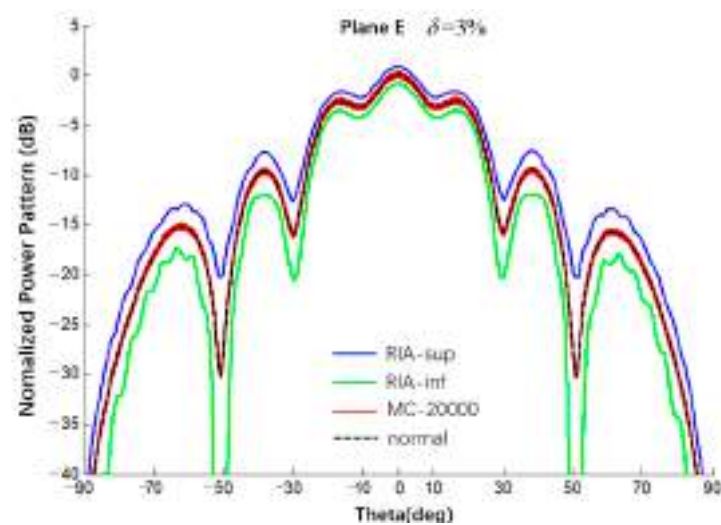


Figure 20. Interval power pattern of excitation amplitude error of spherical CAAs (Plane E, uniform excitation, the tolerance of MC method is 3%).

Table 5. Numerical results of SLL of power pattern in Figures 19 and 20.

Amplitude Error		1%	$\Delta 1\%$	3%	$\Delta 3\%$	5%	$\Delta 5\%$
Main 0 dB	This Work	[−0.29; 0.28]	0.57	[−0.90; 0.83]	1.73	[−1.55; 1.34]	2.89
	MC	[−0.09; 0.09]	0.18	[−0.26; 0.26]	0.52	[−0.44; 0.43]	0.87
1st −2.63 dB	This Work	[−2.95; −2.31]	0.64	[−3.62; −1.68]	1.94	[−4.29; −1.08]	3.21
	MC	[−2.71; −2.54]	0.17	[−2.89; −2.37]	0.52	[−3.07; −2.20]	0.87

4.3. Tolerance Analysis of Spherical CAA with Excitation Phase Error Interval

A uniform excitation occurred, $b_{mn} = 0$, and an error of $\beta\{1, 2, 3\}$ deg was achieved. Compared with the results of the Monte Carlo method, the interval results of the CAA are shown in Figures 21 and 22 and the results are listed in Table 6.

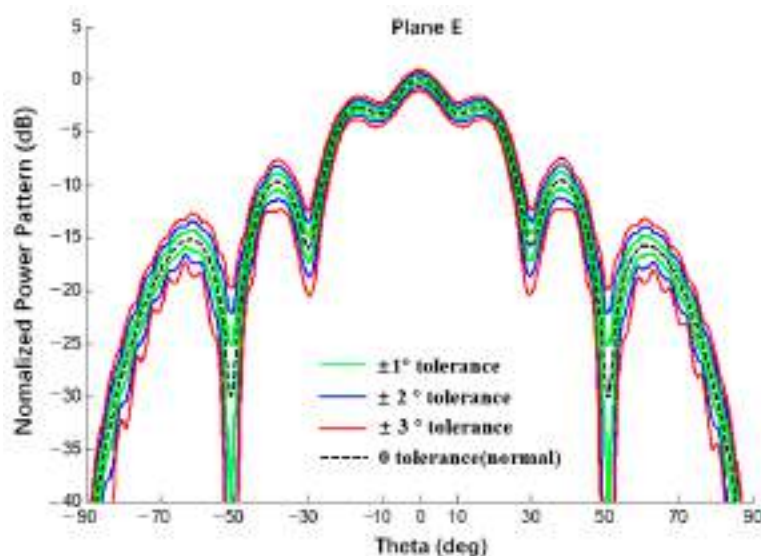


Figure 21. Interval power pattern of excitation phase error of spherical CAAs (Plane E, uniform excitation).

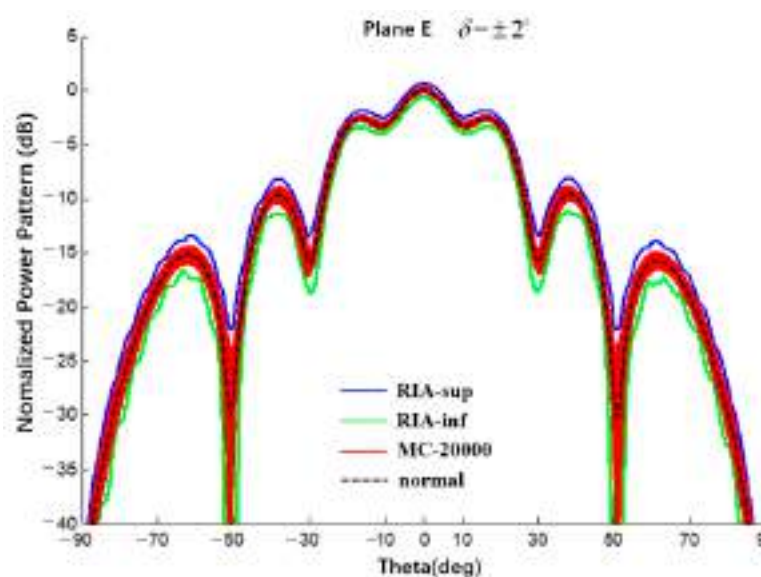


Figure 22. Interval power pattern of excitation phase error of spherical CAAs (Plane E, uniform excitation, the tolerance of MC method is $\pm 2^\circ$).

Table 6. Numerical results of SLL of power pattern in Figures 21 and 22.

Phase Error		1 Deg	$\Delta 1$ Deg	2 Deg	$\Delta 2$ Deg	3 Deg	$\Delta 3$ Deg
Main 0dB	This Work	[−0.33; 0.31]	0.64	[−0.67; 0.61]	1.28	[−1.03; 0.90]	1.93
	MC	[−0.13; 0.13]	0.26	[−0.26; 0.26]	0.52	[−0.41; 0.38]	0.79
1st −2.63dB	This Work	[−3.01; −2.25]	0.76	[−3.41; −1.89]	1.52	[−3.81; −1.54]	2.27
	MC	[−2.75; −2.52]	0.23	[−2.84; −2.42]	0.42	[−2.94; −2.32]	0.62

For the spherical CAAs, the following conclusions can be drawn from the above three numerical examples: (1) when the radius is an interval variable, the width of the interval is the largest; (2) when the MC simulation result is compared with the power pattern, the element factor adopts the surrogate model and the RIA method adopted by the array factor is feasible and the simulation result is valid; (3) all examples verify the envelope of the interval. The premise of the interval analysis method used in this section was to have an explicit expression of the power pattern and to allow some of the variables to be intervalized in order to obtain an intervalized result.

4.4. Spherical CAAs with Different Radii

Taking a linear array of 1×10 as an example, the influence of the curvature radius of the substrate on the electrical performance was calculated through MATLAB when the spherical conformation antenna was studied, as shown in Figure 23. The black dotted line in the figure is the pattern of plane E of the planar array and the other curves are the pattern of the spherical antenna with a radius from 400 mm to 3000 mm.

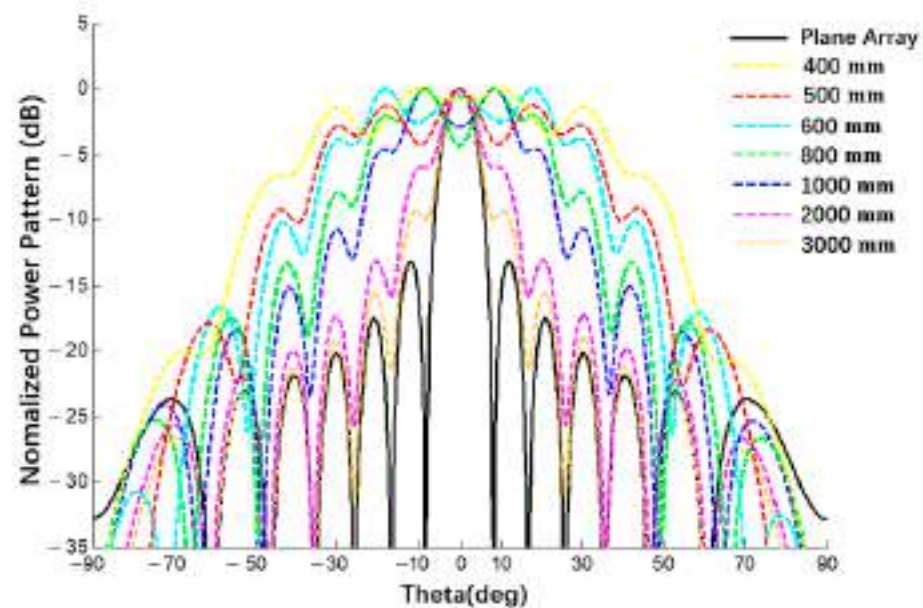


Figure 23. Comparison of the influence of different radii on the pattern when calculated using MATLAB (uniform excitation).

Through a comparison between the patterns of spherical array antennas with different radii and planar array antennas with an increase in radius, the beam width of the power pattern decreases and the pattern of the spherical antenna gradually approaches the pattern of the planar array antenna, which verifies the correctness of the derived expression of the spherical conformal array antenna. In addition, the derived expression can also be used for any array within a spherical range. Examples are shown in Figure 24.

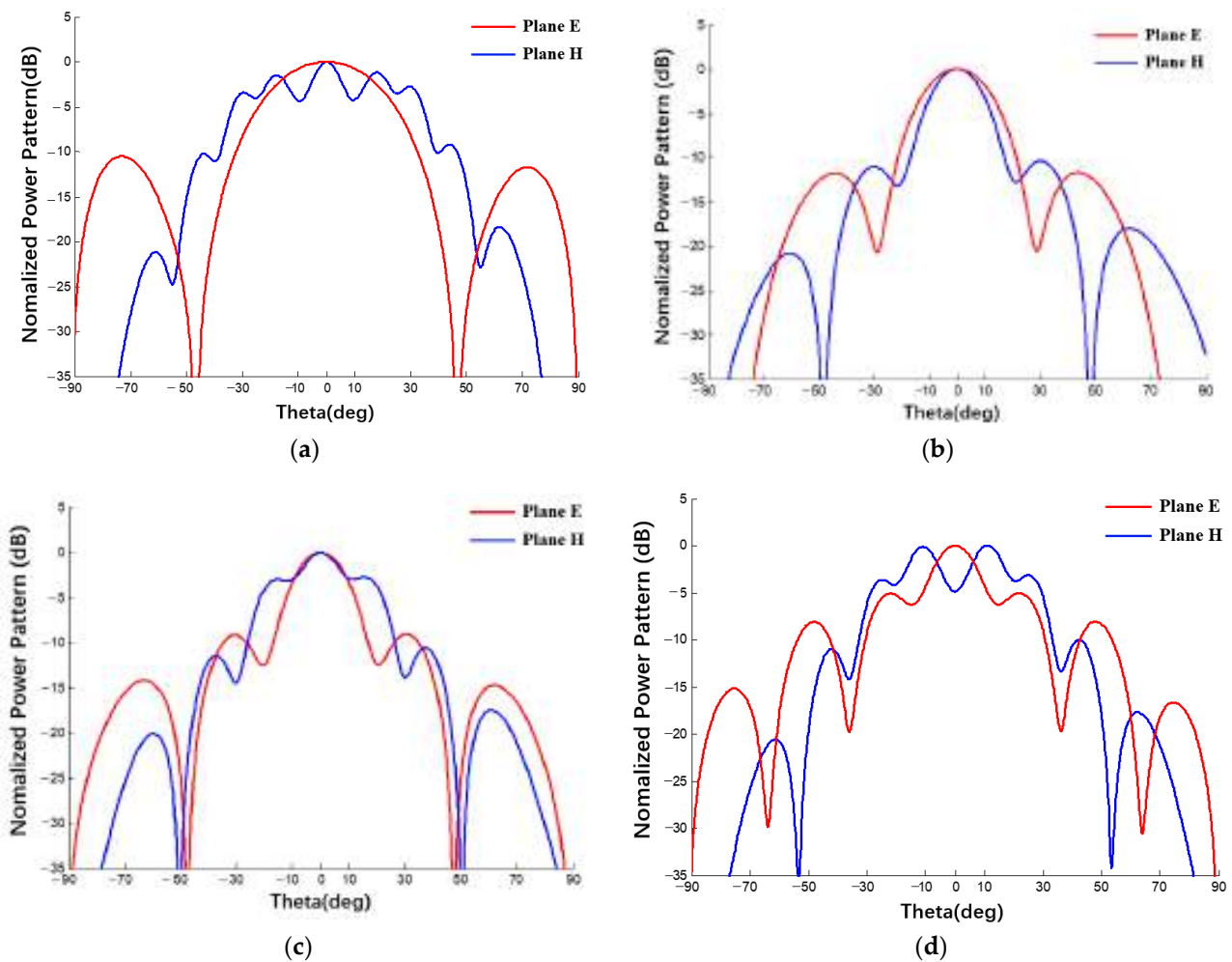


Figure 24. Power patterns of spherical conformal array antennas with different specifications: (uniform excitation, (a) 2×10 , (b) 3×4 , (c) 4×6 , (d) 5×8).

4.5. Influence of Element and Array Factors on Interval of Array Antenna Pattern

In this section, with spherical substrates of the same size ($R_s = 500$ mm) and error (± 0.5 mm), the power patterns of a 1×10 linear array and 10×10 planar array antennas were analyzed using a MATLAB simulation under different conditions to explain the interval influence of the element and array factors on the pattern of the array antenna. As shown in Figures 25 and 26, all curves were calculated using MATLAB. The black line represents the ideal array antenna pattern, the green and red lines are the interval results obtained when only element or array factor errors occur, respectively, and the blue line represents the pattern interval when both the array factor and the array factor error occur simultaneously. It can be seen from the figure that, for both a linear array and a planar array, the pattern interval in which the element and array factor errors occur at the same time envelops the result in which only the array factor error occurs, and the pattern interval in which only the array factor error occurs envelops the result in which only the element factor error occurs.

According to the analysis of the results in Tables 7 and 8, when an error occurs in the radius of the spherical dielectric substrate, the array factor error (coordinate position error of the antenna unit) has a greater impact on the array antenna pattern and the element factor error has a smaller impact on the array antenna pattern but cannot be ignored.

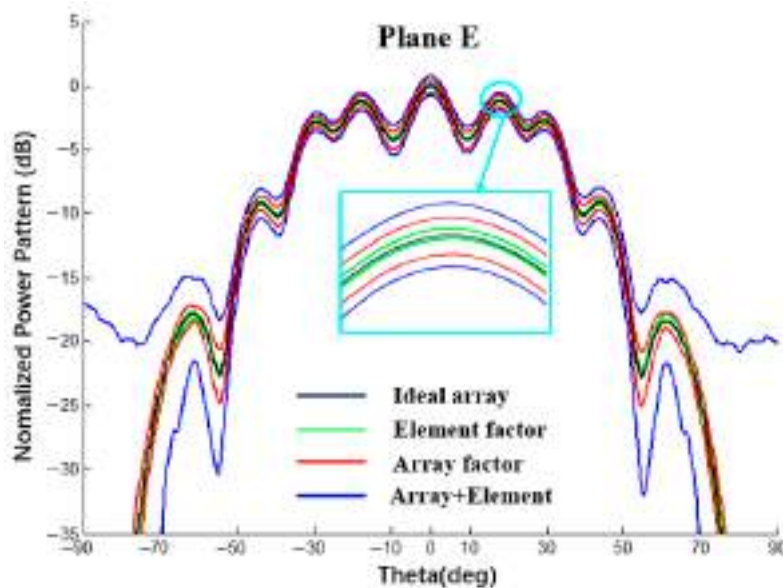


Figure 25. Interval power pattern based on the error of different factors of 1×10 linear arrays (uniform excitation).

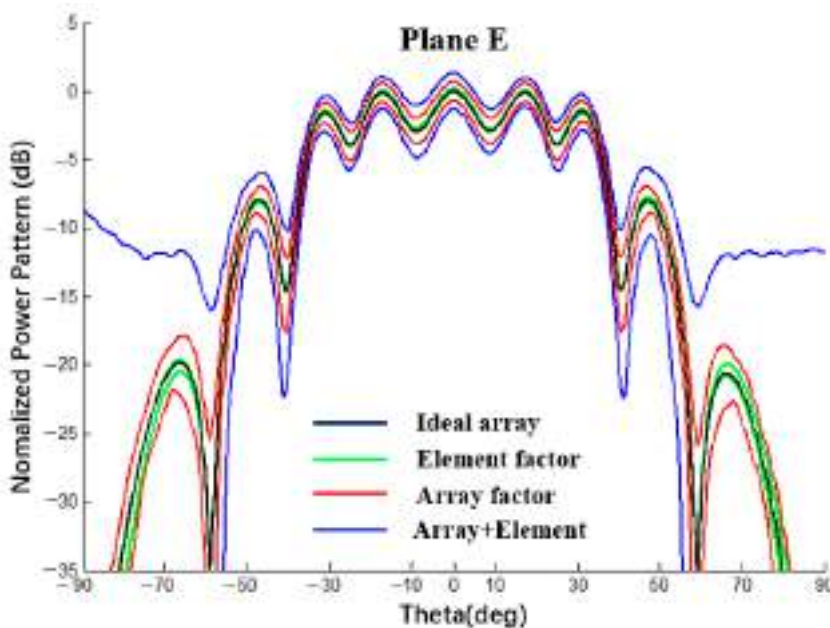


Figure 26. Interval power pattern based on the error of different factors of 10×10 arrays (uniform excitation).

Table 7. SLL interval value in Figure 25 (1×10 linear array).

Lobe	Array + Element Tolerance	ΔAE	Array Factor Tolerance	ΔA	Element Factor Tolerance	ΔE	$\Delta A/\Delta AE$	$\Delta E/\Delta AE$
Main	[-0.76; 0.77]	1.53	[-0.46; 0.43]	0.89	[-0.08; 0.16]	0.24	58.2%	15.7%
1st	[-1.94; -0.52]	1.42	[-1.71; -0.79]	0.92	[-1.29; -1.11]	0.18	64.8%	12.7%
2nd	[-3.51; -2.11]	1.40	[-3.26; -2.39]	0.87	[-2.84; -2.69]	0.15	62.1%	10.7%
3rd	[-10.41; -8.11]	2.30	[-9.75; -8.66]	1.09	[-9.31; -9.08]	0.23	47.4%	10.0%
4th	[-21.55; -14.94]	6.61	[-18.41; -17.20]	1.21	[-18.29; -17.68]	0.61	18.3%	9.2%

Table 8. SLL interval value in Figure 26 (10×10 array).

Lobe	Array + Element Tolerance	ΔAE	Array Factor Tolerance	ΔA	Element Factor Tolerance	ΔE	$\Delta A/\Delta AE$	$\Delta E/\Delta AE$
Main	[−1.33; 1.32]	2.65	[−0.68; 0.68]	1.36	[−0.08; 0.16]	0.24	51.3%	9.1%
1st	[−1.26; 1.08]	2.34	[−0.80; 0.59]	1.39	[−0.16; 0.03]	0.19	59.4%	8.1%
2nd	[−2.90; −0.27]	2.63	[−2.30; −0.82]	1.48	[−1.61; −1.42]	0.19	56.3%	7.2%
3rd	[−10.12; −5.92]	4.20	[−8.90; −6.98]	1.92	[−8.10; −7.86]	0.24	45.7%	5.7%

5. Conclusions

This study follows the surrogate model method for an element factor and the interval calculation method for the real and imaginary parts of an array factor. The following conclusions can be drawn from the analysis of the power pattern interval of the non-expandable spherical CAA:

(1) When the radius is an interval variable, the interval width is the largest; thus, the proportion of the interval radius is reduced, the remaining error is a few percentage points, and the radius is a few tenths of a percent.

(2) Compared with the Monte Carlo method, the method used in an interval analysis can effectively, simply, and reasonably solve the influence of the spherical substrate radius error and the excitation amplitude and phase error on the pattern.

(3) The object of this article is a spherical CAA that has not been analyzed for the interval and provides new material for the development of an interval analysis in the field of antennas.

(4) For explicit expressions that are difficult to derive directly, surrogate models or machine learning algorithms can be used to solve them. This research uses the BP intelligent algorithm to build the surrogate model; other artificial intelligence algorithms are also suitable for this research.

Author Contributions: Conceptualization, G.D. and P.L.; methodology, P.R.; validation, J.C. and P.R.; software, G.D. and W.X.; writing—original draft preparation, G.D.; writing—review and editing, P.L. and P.R.; visualization, J.C. and W.X.; project administration, P.L.; funding acquisition, P.L. All authors have read and agreed to the published version of the manuscript.

Funding: This work was supported by the National Natural Science Foundation of China (Grant No. 51875431 and No. 61971334), the Natural Science Basic Research Plan in Shaanxi Province (2022JC-33, Grant 2021JZD-003, and Grant 2018TD-012), the Fundamental Research Funds for the Central Universities, and the National 111 Project.

Institutional Review Board Statement: Not applicable.

Informed Consent Statement: Not applicable.

Data Availability Statement: Not applicable.

Acknowledgments: We are very grateful to Chao Wang for his fundamental analysis of the uncertainty factors of the patch antenna element, which provided the direction and method for our research. He is currently working in the Antenna and Servo Department, the 54th Research Institute, China Electronics Technology Group Corporation, Shijiazhuang, He Bei Province 050081, China.

Conflicts of Interest: The authors declare no conflict of interest. The funders had no role in the design of the study; in the collection, analyses, or interpretation of data; in the writing of the manuscript; or in the decision to publish the results.

References

- Albagory, Y. An Efficient Conformal Stacked Antenna Array Design and 3D-Beamforming for UAV and Space Vehicle Communications. *Sensors* **2021**, *21*, 1362. [[CrossRef](#)] [[PubMed](#)]
- Ogurtsov, S.; Koziel, S. A Conformal Circularly Polarized Series-Fed Microstrip Antenna Array Design. *IEEE Trans. Antennas Propag.* **2019**, *68*, 873–881. [[CrossRef](#)]

3. Pelham, T.; Hilton, G.; Mellios, E.; Lewis, R. Predicting Conformal Aperture Gain From 3-D Aperture and Platform Models. *IEEE Antennas Wirel. Propag. Lett.* **2017**, *16*, 700–703. [[CrossRef](#)]
4. Jilani, S.F.; Munoz, M.O.; Abbasi, Q.H.; Alomainy, A. Millimeter-Wave Liquid Crystal Polymer Based Conformal Antenna Array for 5G Applications. *IEEE Antennas Wirel. Propag. Lett.* **2019**, *18*, 84–88. [[CrossRef](#)]
5. Yang, H.; Liu, X.; Fan, Y. Design of Broadband Circularly Polarized All-Textile Antenna and Its Conformal Array for Wearable Devices. *IEEE Trans. Antennas Propag.* **2021**, *70*, 209–220. [[CrossRef](#)]
6. Peng, J.-J.; Qu, S.-W.; Xia, M.; Yang, S. Conformal Phased Array Antenna for Unmanned Aerial Vehicle With $\pm 70^\circ$ Scanning Range. *IEEE Trans. Antennas Propag.* **2021**, *69*, 4580–4587. [[CrossRef](#)]
7. Chapman, A.J.; Fenn, A.J.; Dufilie, P. Compact Cavity-Backed Discone Array for Conformal Omnidirectional Antenna Applications. In Proceedings of the 2020 IEEE International Symposium on Antennas and Propagation and North American Radio Science Meeting, Montreal, QC, Canada, 5–10 July 2020; pp. 657–658.
8. Hussain, S.; Qu, S.; Zhang, P.; Wang, X.; Yang, S. A Low-Profile, Wide-Scan, Cylindrically Conformal X-Band Phased Array. *IEEE Antennas Wirel. Propag. Lett.* **2021**, *20*, 1503–1507. [[CrossRef](#)]
9. Lin, H.S.; Cheng, Y.J.; Wu, Y.F.; Fan, Y. Height Reduced Concave Sector-Cut Spherical Conformal Phased Array Antenna Based on Distributed Aperture Synthesis. *IEEE Trans. Antennas Propag.* **2021**, *69*, 6509–6517. [[CrossRef](#)]
10. Boyuan, M.; Pan, J.; Wang, E.; Luo, Y. Conformal Bent Dielectric Resonator Antennas With Curving Ground Plane. *IEEE Trans. Antennas Propag.* **2019**, *67*, 1931–1936. [[CrossRef](#)]
11. Ramadan, M.; Dahle, R. Characterization of 3-D Printed Flexible Heterogeneous Substrate Designs for Wearable Antennas. *IEEE Trans. Antennas Propag.* **2019**, *67*, 2896–2903. [[CrossRef](#)]
12. Wang, C.; Li, P.; Xu, W.; Song, L.; Huang, J. Tolerance analysis of 3D printed patch antennas based on interval arithmetic. *Microw. Opt. Technol. Lett.* **2020**, *63*, 516–524. [[CrossRef](#)]
13. Rocca, P.; Anselmi, N.; Benoni, A.; Massa, A. Probabilistic Interval Analysis for the Analytic Prediction of the Pattern Tolerance Distribution in Linear Phased Arrays With Random Excitation Errors. *IEEE Trans. Antennas Propag.* **2020**, *68*, 7866–7878. [[CrossRef](#)]
14. He, G.; Gao, X.; Zhou, H. Matrix-Based Interval Arithmetic for Linear Array Tolerance Analysis With Excitation Amplitude Errors. *IEEE Trans. Antennas Propag.* **2019**, *67*, 3516–3520. [[CrossRef](#)]
15. Ruze, J. The effect of aperture errors on the antenna radiation pattern. *Il Nuovo Cimento* **1952**, *9*, 364–380. [[CrossRef](#)]
16. Ruze, J. Antenna tolerance theory—A review. *Proc. IEEE* **1996**, *54*, 633–640. [[CrossRef](#)]
17. Gilbert, E.N.; Morgan, S.P. Optimum Design of Directive Antenna Arrays Subject to Random Variations. *Bell Syst. Tech. J.* **1955**, *34*, 637–663. [[CrossRef](#)]
18. Elliott, R. Mechanical and electrical tolerances for two-dimensional scanning antenna arrays. *IRE Trans. Antennas Propag.* **1958**, *6*, 114–120. [[CrossRef](#)]
19. Rahmat-Samii, Y. An efficient computational method for characterizing the effects of random surface errors on the average power pattern of reflectors. *IEEE Trans. Antennas Propag.* **1983**, *31*, 92–98. [[CrossRef](#)]
20. Ling, H.; Lo, Y.; Rahmat-Samii, Y. Reflector sidelobe degradation due to random surface errors. *IRE Trans. Antennas Propag.* **1986**, *34*, 164–172. [[CrossRef](#)]
21. Hsiao, J.K. Normalized relationship among errors and sidelobe levels. *Radio Sci.* **1984**, *19*, 292–302. [[CrossRef](#)]
22. Hsiao, J. Design of error tolerance of a phased array. *Electron. Lett.* **1985**, *21*, 834–836. [[CrossRef](#)]
23. Rocca, P. Interval arithmetic for pattern tolerance analysis of parabolic reflectors. *IEEE Trans. Antennas Propag.* **2014**, *62*, 4952–4960. [[CrossRef](#)]
24. Rocca, P.; Manica, L.; Massa, A. Interval-based analysis of pattern distortions in reflector antennas with bump-like surface deformations. *IET Microwaves, Antennas Propag.* **2014**, *8*, 1277–1285. [[CrossRef](#)]
25. Anselmi, N.; Manica, L.; Rocca, P.; Massa, A. Tolerance analysis of reconfigurable monopulse linear antenna arrays using interval arithmetic. In Proceedings of the 8th European Conference on Antennas and Propagation, The Hague, The Netherlands, 6–11 April 2014; pp. 1509–1512. [[CrossRef](#)]
26. Anselmi, N.; Salucci, M.; Rocca, P.; Massa, A. Generalised interval-based analysis tool for pattern distortions in reflector antennas with bump-like surface deformations. *IET Microwaves, Antennas Propag.* **2016**, *10*, 909–916. [[CrossRef](#)]
27. Carlin, M.; Anselmi, N.; Manica, L.; Rocca, P.; Massa, A. Exploiting Interval Arithmetic for predicting real arrays performances—The linear case. In Proceedings of the IEEE International Symposium on Antennas and Propagation & USNC/URSI National Radio Science Meeting, Orlando, FL, USA, 7–13 July 2013; pp. 298–299.
28. Anselmi, N.; Manica, L.; Rocca, P.; Massa, A. Tolerance Analysis of Antenna Arrays Through Interval Arithmetic. *IEEE Trans. Antennas Propag.* **2013**, *61*, 5496–5507. [[CrossRef](#)]
29. Rocca, P.; Manica, L.; Anselmi, N.; Massa, A. Analysis of the Pattern Tolerances in Linear Arrays With Arbitrary Amplitude Errors. *IEEE Antennas Wirel. Propag. Lett.* **2013**, *12*, 639–642. [[CrossRef](#)]
30. Poli, L.; Rocca, P.; Anselmi, N.; Massa, A. Dealing With Uncertainties on Phase Weighting of Linear Antenna Arrays by Means of Interval-Based Tolerance Analysis. *IEEE Trans. Antennas Propag.* **2015**, *63*, 3229–3234. [[CrossRef](#)]
31. Anselmi, N.; Salucci, M.; Rocca, P.; Massa, A. Power Pattern Sensitivity to Calibration Errors and Mutual Coupling in Linear Arrays through Circular Interval Arithmetics. *Sensors* **2016**, *16*, 791. [[CrossRef](#)]
32. Li, P.; Xu, W.; Yang, D. An Inversion Design Method for the Radome Thickness Based on Interval Arithmetic. *IEEE Antennas Wirel. Propag. Lett.* **2018**, *17*, 658–661. [[CrossRef](#)]

33. Li, P.; Pedrycz, W.; Xu, W.; Song, L. Far-Field Pattern Tolerance Analysis of the Antenna-Radome System With the Material Thickness Error: An Interval Arithmetic Approach. *IEEE Trans. Antennas Propag.* **2017**, *65*, 1934–1946. [[CrossRef](#)]
34. Li, P.; Wang, C.; Xu, W.; Song, L. Taylor Expansion and Matrix-Based Interval Analysis of Linear Arrays With Patch Element Pattern Tolerance. *IEEE Access* **2021**, *9*, 21004–21015. [[CrossRef](#)]
35. Balanis, C.A. *Antenna Theory: Analysis and Design*, 3rd ed.; Harper & Row: New York, NY, USA, 1982.
36. Josefsson, L.; Persson, P. *Conformal Array Antenna Theory and Design*; Wiley: Hoboken, NJ, USA, 2006; pp. 17–20. [[CrossRef](#)]
37. Hu, N.; Duan, B.; Xu, W.; Zhou, J. A New Interval Pattern Analysis Method of Array Antennas Based on Taylor Expansion. *IEEE Trans. Antennas Propag.* **2017**, *65*, 6151–6156. [[CrossRef](#)]
38. Chaudhary, V.; Panwar, R. FSS Derived Using a New Equivalent Circuit Model Backed Deep Neural Network. *IEEE Antennas Wirel. Propag. Lett.* **2021**, *20*, 1963–1967. [[CrossRef](#)]
39. Gargantini, I.; Henrici, P. Circular arithmetic and the determination of polynomial zeros. *Numer. Math.* **1971**, *18*, 305–320. [[CrossRef](#)]